2-D Ultrasound Sparse Arrays Multidepth Radiation Optimization Using Simulated Annealing and Spiral-Array Inspired Energy Functions

Emmanuel Roux, *Student Member, IEEE*, Alessandro Ramalli, *Member, IEEE*, Piero Tortoli, *Senior Member, IEEE*, Christian Cachard, Marc C. Robini, and Hervé Liebgott, *Associate Member, IEEE*

***Abstract*— Full matrix arrays are excellent tools for 3-D ultrasound imaging, but the required number of active elements is too high to be individually controlled by an equal number of scanner channels. The number of active elements is significantly reduced by the sparse array techniques, but the position of the remaining elements must be carefully optimized. This issue is faced here by introducing novel energy functions in the simulated annealing (SA) algorithm. At each iteration step of the optimization process, one element is freely translated and the associated radiated pattern is simulated. To control the pressure field behavior at multiple depths, three energy functions inspired by the pressure field radiated by a Blackman-tapered spiral array are introduced. Such energy functions aim at limiting the main lobe width while lowering the side lobe and grating lobe levels at multiple depths. Numerical optimization results illustrate the influence of the number of iterations, pressure measurement points, and depths, as well as the influence of the energy function definition on the optimized layout. It is also shown that performance close to or even better than the one provided by a spiral array, here assumed as reference, may be obtained. The finite-time convergence properties of SA allow the duration of the optimization process to be set in advance.**

***Index Terms*— 3-D, optimization, simulated annealing (SA), sparse arrays, transducers, ultrasound (US).**

Manuscript received January 19, 2016; accepted August 19, 2016. Date of publication August 24, 2016; date of current version December 1, 2016. This work was supported in part by la Région Rhône-Alpes under Grant CMIRA 2014, in part by Université Franco-Italienne under Grant VINCI 2014, C2-13, in part by the European Union through the ENIAC JU Project DeNeCoR under Grant 324257, and in part by (a PALSE Mobility Grant) by the framework of the LABEX CELYA (ANR-10-LABX-0060) and LABEX PRIMES (ANR-11-LABX-0063) of Université de Lyon, within the Program Investissements d'Avenir (ANR-11-IDEX-0007) operated by the French National Research Agency. *(Corresponding author: Emmanuel Roux.)*

E. Roux is with the Department of Information Engineering, Università degli Studi di Firenze, Florence 50139, Italy, also with the Centre de Recherche en Applications et Traitement de l'image pour la Santé, Institut national de la santé et de la recherche médicale and the Institut national des sciences appliquées de Lyon, Université de Lyon, 69007 Lyon, France, and also with the Université Claude Bernard Lyon 1, Villeurbanne 69100, France (e-mail: roux@creatis.univ-lyon1.fr).

A. Ramalli and P. Tortoli are with the Department of Information Engineering, Università degli Studi di Firenze, 50139 Firenze, Italy (e-mail: alessandro.ramalli@unifi.it; piero.tortoli@unifi.it).

C. Cachard, M. C. Robini, and H. Liebgott are with the Centre de Recherche en Applications et Traitement de l'image pour la Santé, Institut national de la santé et de la recherche médicale and the Institut national des sciences appliquées de Lyon, Université de Lyon, 69007 Lyon, France, and also with the Université Claude Bernard Lyon 1, Villeurbanne 69100, France (e-mail: cachard@creatis.univ-lyon1.fr; robini@creatis.insa-lyon.fr; liebgott@creatis.univ-lyon1.fr).

Digital Object Identifier 10.1109/TUFFC.2016.2602242

I. Introduction

THREE-DIMENSIONAL ultrasound (3-D US) imaging systems allow scanning the volume of interest using mechanically translated/tilted/rotated single-element/linear/phased/convex array probes [1]–[3] or 2-D matrix array probes [4], [5]. The latter ones overcome the limitations of stepper motors in terms of achievable frame rate [1] and calibration issues [6] by performing 3-D electronic steering and focusing of the US beam. Moreover, 2-D arrays enable ultrafast imaging [7], [8] by the transmission of plane or diverging waves, which can also be combined to improve contrast and resolution.

The availability of volumetric information allowed introducing innovative applications for elastography [9], [10], tissue Doppler, and blood flow analysis [11], as well as for surgery by intraoperative visualization, biopsy needle tracking [12], [13], and in therapeutic high intensity focused US (HIFU) intervention monitoring [14], [15]. Two-dimensional arrays for 3-D imaging systems are already available for research purposes [7], [16]–[19], but full arrays respecting the $\lambda/2$ space sampling constraint to ensure low grating lobes require thousands of active elements. The individual control of so many elements would dramatically increase the system cost and power consumption, the size of the probe cable, and the real-time processing load. Promising solutions are the microbeamforming [20]–[23], row-column addressing [19], [24], [25], or channel multiplexing [4] techniques. However, these techniques imply embedding in the probe application-specific integrated circuits (ASICs), having stringent requirements in terms of dimension, power dissipation, and cost, which have been satisfied in a few hi-end commercial systems [26]–[28].

As an alternative to probes integrating an ASIC, sparse array techniques reduce the number of active elements while trying to maintain acceptable performance in terms of grating lobes, resolution, and sensitivity. Such performance is strictly associated with the positions and dimensions of the active elements, which can be defined by means of deterministic or stochastic methods. The former ones have led to planar Vernier arrays [29], regular and radially periodic arrays [30], and, more recently, to density tapered spiral arrays [31], [32]. The 30λ-radius Blackman-tapered spiral array having

1.0λ-size elements is assumed as reference in this paper because it offered the best compromise for small-vessel imaging among the 105 configurations tested in [32].

Searching for an optimum among all possible sparse array configurations is a very large scale combinatorial problem that suggests the use of stochastic optimization methods such as genetic algorithm [33], [34] and simulated annealing (SA) [30], [35]–[41]. In these approaches, the choice of the energy function that controls the optimization process is often based on a beam pattern aiming at reducing the side lobe level (SLL) and grating lobe level (GLL) while maintaining a narrow main lobe. In order to reduce the computation time (a drawback of stochastic optimization), the beam pattern is generally computed by assuming the far-field approximation in the analytical model. Choe *et al.* [42] introduced a more realistic acoustic simulation of the pressure field using the FIELD II software [43], [44], but they assumed horizontal and vertical symmetry and the element positions were restricted to a 16×16 regular grid.

In this paper, we present a new sparse array design strategy that optimizes the pressure field at several depths by permitting arbitrary positions of the array elements over the entire aperture. In particular, such positions are optimized by an SA algorithm implementation that integrates fast simulations of the pressure field [45]. The elements can arbitrarily move on the layout during the optimization process, and the associated beam patterns are calculated for each new solution. In order to control the behavior at multiple depths, the pressure field was simulated over three concentric hemispheres. Moreover, three innovative multidepth energy functions, inspired by the Blackman-tapered spiral array performance, are introduced.

This paper is organized as follows. Section II presents the mathematical formalism that models the problem and the proposed energy functions. Section III shows sample results of optimized 256-element arrays, which are discussed in Section IV. Concluding remarks are given in Section V.

II. Methods

A. 2-D Sparse Arrays Optimization Model

The 2-D sparse array optimization problem is formulated as the minimization of an energy function U on a finite state space Ω. This is performed by a Metropolis-type SA [46], [47] algorithm that is a Markov chain $(S_n)_{n\in\mathbb{N}}$ on Ω whose transitions are guided by a communication mechanism Θ and controlled by a cooling sequence $(\beta_n)_{n\in\mathbb{N}}$ (see [48], [49]).

1) State Space: The state space Ω of the possible solutions S in which an optimal configuration S_{opti} has to be found is the set of planar 2-D sparse arrays with N_{e} nonoverlapping active elements in a disk of radius r_{p}. The degrees of freedom are the element positions (x_k, y_k) on a fine Cartesian grid G superimposed on the disk of radius r_{p}. Hence, Ω is defined by

$$\Omega = \{((x_1, y_1), \ldots, (x_{N_{\text{e}}}, y_{N_{\text{e}}})) \in G^{N_{\text{e}}} | \text{A}_i \cap \text{A}_j = \emptyset, \text{ for all } i, j \in [1 \ldots N_{\text{e}}] \text{ such that } i \neq j\} \quad (1)$$

where A_k is the area occupied by the kth element broadened of a $\lambda/20$ safeguard margin in each direction assuming that below such an interelement distance the electro-acoustic coupling effect (crosstalk) would be too high to separate the elements [50]. (In practice, the grid spacing has no impact on the outputs as long as it is smaller than $\sim \lambda/100$.) The minimum interelement distance may also be parameterized according to the technology used to build the active elements in order to respect the constraints of the manufacturing process.

2) Communication Mechanism: During the exploration of Ω, the transition from a state S to a new candidate $\tilde{S}$ was controlled by the communication mechanism Θ [49]. The communication mechanism $\Theta : \Omega \to [0, 1]$ was defined using the standard construction scheme based on a neighborhood $\mathcal{G}(S)$ that specifies the allowed moves from S to $\tilde{S}$

$$\Theta(S, \tilde{S}) = \begin{cases} \dfrac{1}{N_{\text{e}} \cdot |G|}, & \text{if } \tilde{S} \in \mathcal{G}(S) \\ 1 - \dfrac{1}{N_{\text{e}} \cdot |G|}|\mathcal{G}(S)|, & \text{if } \tilde{S} = S \\ 0, & \text{otherwise} \end{cases} \quad (2)$$

where $\mathcal{G}(S)$ is given by

$$\mathcal{G}(S) = \{\tilde{S} \in \Omega | \exists! k \in [1 \ldots N_e], \tilde{S}(k) \neq S(k)\} \cap \{\tilde{S} \in \Omega | \exists! k \in [1 \ldots N_e], \quad 0 < \|\tilde{S}(k) - S(k)\|_2 < t_r\} \quad (3)$$

where $S(k)$ denotes the kth element coordinates (x_k, y_k) and t_{r} is the maximum translation value.

In other words, the neighborhood $\mathcal{G}(S)$ is the set of arrays in Ω with only one translated element with respect to S and $\Theta(S, \tilde{S})$ generates a candidate $\tilde{S}$ from the current state S by translating a single element by a distance in $]0, t_{\text{r}}[$. According to definition (3), Θ satisfies the symmetry and irreducibility conditions [49], which allow us to define the transition matrix $\text{P}(S_{n+1}|S_n)$ of the SA Markov chain $(S_n)_{n\in\mathbb{N}}$

$$\text{P}(S_{n+1} = \tilde{S} | S_n = S) = \begin{cases} \Theta(S, \tilde{S}), & \text{if } \Delta U \leq 0 \text{ and } \tilde{S} \neq S \\ \Theta(S, \tilde{S}) e^{-\beta_n \Delta U}, & \text{if } \Delta U > 0 \end{cases} \quad (4)$$

where $\Delta U = U(\tilde{S}) - U(S)$ is the energy variation associated with the transition $S \to \tilde{S}$. During the optimization process, the probability to accept a given transition with positive energy variation is $\exp(-\beta_n \Delta U)$ and is called the acceptation rate. This acceptation rate is controlled by the cooling sequence $(\beta_n)_{n\in\mathbb{N}}$, which has the general form

$$\beta_n = \beta_{\text{inf}} \left(\frac{\beta_{\text{sup}}}{\beta_{\text{inf}}} \right)^{\frac{1}{\sigma - 1}\left(\left\lceil \frac{n}{K} \right\rceil - 1\right)} \quad (5)$$

where β_{inf} is the initial inverse temperature, β_{sup} is the final inverse temperature, and σ is the number of constant temperature stages, each of length K (so the total number of iterations is $N_{\text{iter}} = \sigma K$).

3) Energy Function:

a) Space sampling: To compute the normalized radiated pattern $\text{RP}_{S_n}(R, \theta, \phi)$ of the array S_n at iteration n, the associated pressure field PF_{S_n} is first simulated using FIELD II [43], [44]

$$\text{RP}_{S_n}(R, \theta, \phi) = \frac{\max_t \text{PF}_{S_n}(R, \theta, \phi, t)}{\max_{\theta,\phi,t} \text{PF}_{S_n}(R, \theta, \phi, t)} \quad (6)$$

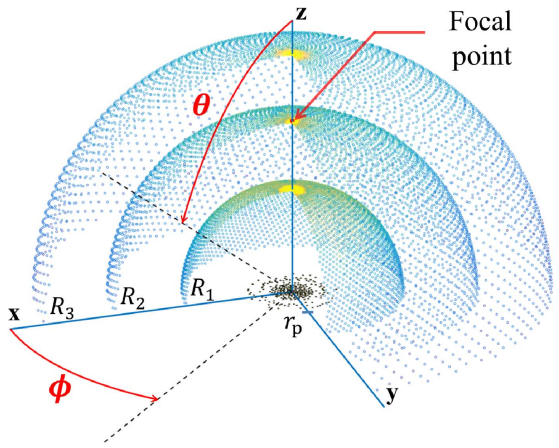

Fig. 1. Reference coordinate system for the three hemispheres of radius R_1, R_2, and R_3, each used to estimate the pressure in 5000 PMPs. The 2-D sparse array probe of radius r_p is centered on the origin of the axes. The focal point is on the z-axis at depth $z = R_2$.

where $\mathrm{PF}_{S_n}(R, \theta, \phi, t)$ is the one-way pressure field of S_n depending on spherical coordinates (R, θ, ϕ) and time t, the origin of which is the center of the probe layout (Fig. 1).

Asspecified in [45], in order to simulate $\mathrm{PF}_{S_n}(R, \theta, \phi, t)$, N_{PMP} pressure measurement points (PMPs) were positioned on a 3-D spiral arm laying on N_{H} hemispheres of radius $R_1, \ldots, R_{N_{\mathrm{H}}}$ (Fig. 1) so that no periodicity is introduced (or hidden) in the measurements.

b) Energy function expressions: The common goal of the three energy functions U_1, U_2, and U_3 defined below is to obtain a good resolution and contrast in the image. In other words, they are aimed at minimizing the SLL and GLL beyond the main lobe that has a fixed width $\theta_{\mathrm{ML}}(R)$ chosen as the -30 dB main lobe width of the spiral array [32] beam pattern at depth R.

The energy function U_1 is the square of the maximum of pressure outside the main lobe region at depth R

$$U_{1,R}(S_n) = \left(\max_{(\theta,\phi),\notin L} (\mathrm{RP}_{S_n}(R, \theta, \phi)) \right)^2 \tag{7}$$

where $L = \{(\theta, \phi) | \theta < ((\theta_{\mathrm{ML}}(R))/2)\}$ is the main lobe region delimited by half of $\theta_{\mathrm{ML}}(R)$.

The energy function U_2 is the product of U_1 with the squared pressure ratio at depth R

$$U_{2,R}(S_n) = U_{1,R}(S_n) \left(\frac{\mathrm{P}_{\mathrm{out}}(R)}{\mathrm{P}_{\mathrm{in}}(R)} \right)^2 \tag{8}$$

with

$$\mathrm{P}_{\mathrm{out}}(R) = \iint_{(\theta,\phi)\notin L} (\mathrm{RP}_{S_n}(R, \theta, \phi)) \mathrm{d}\theta \mathrm{d}\phi \tag{9}$$

and

$$\mathrm{P}_{\mathrm{in}}(R) = \iint_{(\theta,\phi)\in L} (\mathrm{RP}_{S_n}(R, \theta, \phi)) \mathrm{d}\theta \mathrm{d}\phi. \tag{10}$$

For the energy function U_3, a sculpting mask q_{mask} is defined as follows:

$$q_{\mathrm{mask}}(R, \theta, \phi) = \begin{cases} \mathrm{IFT}(\mathrm{Blackman}(r_p)), & \text{if } (\theta, \phi) \in L \\ 0, & \text{if } (\theta, \phi) \notin L. \end{cases} \tag{11}$$

In other words, inside the main lobe region L, the sculpting mask q_{mask} is given by the inverse Fourier Transform of the Blackman window applied to a disk of radius r_{p}, and outside the main lobe region, the mask is set to zero. The introduction of such a sculpting mask creates a new constraint in the main lobe region: the main lobe shape must fit under the main lobe of the Blackman-tapered spiral array [32]. The motivation to sculpt the main lobe shape is to better control the beam profile and avoid undesired lobes inside the main lobe region. The constraint outside the main lobe region is still to reach the minimum GLL and SLL: the sculpting mask is set to zero in this region. The energy function U_3 is the square of the product between the pressure ratio $\mathrm{P}_{\mathrm{out}}/\mathrm{P}_{\mathrm{in}}$ and the maximum positive pressure difference with q_{mask}

$$U_{3,R}(S_n) = \left(M_{\mathrm{q}} \frac{\mathrm{P}_{\mathrm{out}}(R)}{\mathrm{P}_{\mathrm{in}}(R)} \right)^2 \tag{12}$$

where

$$M_{\mathrm{q}} = \max[\max_{\theta,\phi} \mathrm{RP}_{S_n}(R, \theta, \phi) - q_{\mathrm{mask}}(R, \theta, \phi), 0]. \tag{13}$$

In summary, U_1 measures the maximum of pressure outside the main lobe region L, U_2 combines U_1 with the pressure ratio $(\mathrm{P}_{\mathrm{out}}(R))/(\mathrm{P}_{\mathrm{in}}(R))$, and U_3 combines U_2 with a mask sculpting the main lobe shape.

c) Multidepth pressure field control: Our method allows adding hemispheres of PMPs to take into account the pressure field behavior below and above the focal depth in the optimization (example with three hemispheres in Fig. 1). Multidepth energy functions can be defined, and the acoustic radiation patterns of the array can be optimized using simulations performed at different depths. It represents a first step toward an optimization of the 3-D pressure field. The multidepth pressure field control is further discussed in Section IV-C.

When N_{H} hemispheres of PMPs are considered, the overall energy function is the sum of the energy functions associated with each hemisphere

$$U^{N_{\mathrm{H}}}(S_n) = \sum_{i=1}^{N_{\mathrm{H}}} U_{R_i}(S_n). \tag{14}$$

B. Simulated Annealing Algorithm

The difficulty of the optimization problem is beyond the capabilities of deterministic algorithms. Indeed, the considered energy functions generate complex landscapes with deep local basins of attraction and are defined on a huge configuration space. This advocates the use of a stochastic optimization such as SA [46]–[49].

The SA flowchart is given in Fig. 2: the first step (A) consists in choosing an initial solution S_0 and computing the initial pressure field $\mathrm{PF}_{S_0}(R, \theta, \phi, t)$ and associated energy $U(S_0)$. The initial and final inverse temperatures β_{inf} and β_{sup} are computed during step (A) using the methods described in [48] and [49]. A new solution $\tilde{S}_n$ is proposed in (B) using the communication mechanism Θ described in Section II-A. The pressure field simulations in step (C) are very time consuming when using FIELD II, limiting the achievable N_{iter} performed in a reasonable and acceptable computing time

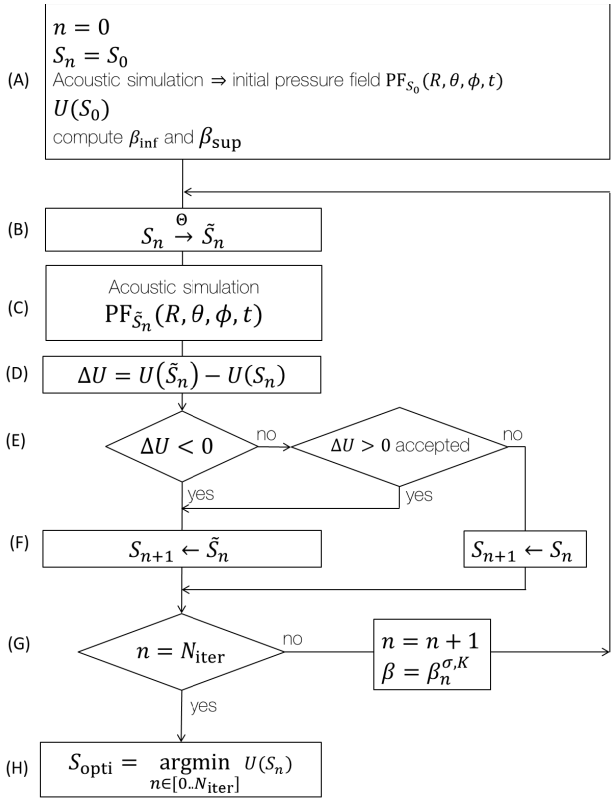

Fig. 2. SA flowchart.

(e.g., some weeks). To reduce the pressure field computation time and hence increase the number of iterations that can be performed, an ergonomic update of the pressure field is implemented as described in [45]. The energy difference between the current solution S_n and the new proposal $\tilde{S}_n$ is computed in step (D) as ΔU. In step (E), $\tilde{S}_n$ is accepted with probability $\exp(-\beta_n \Delta U)$. In step (F), the next iterate S_{n+1} is either updated to $\tilde{S}_n$ or set to S_n, depending on the decision taken in step (E). In step (G), if the number of planned iterations N_{iter} is not reached, the iteration index and the inverse-temperature value are updated. In step (H), the best solution (i.e., with the lowest energy value) encountered during the optimization process is stored as the optimized solution S_{opti}.

C. Postoptimization Performance Evaluation With 3-D Simulations

1) Performance Metrics: Three-dimensional one-way pressure fields were simulated in a Three-dimensional volume ($L_x \times L_y \times L_z = 40 \times 40 \times 30$ mm^3), compatible with peripheral vessel imaging, for each of the optimized array as performed in [32]. The simulated volume was centered over the array starting at depth $z = 10$ mm, and it was sampled with a voxel resolution of $v_{\mathrm{res}} = \delta x \times \delta y \times \delta z = 132\ \mu\mathrm{m} \times 132\ \mu\mathrm{m} \times 264\ \mu\mathrm{m} = 0.43\lambda^3$. For each solution, 81 steering angles ($\theta_{\mathrm{zx}} = -32{:}8{:}+32°$, $\theta_{\mathrm{zy}} = -32{:}8{:}+32°$) were considered, and for each simulation, the array performance was assessed through the following six parameters [32].

TABLE I
SIMULATION PARAMETERS

Acoustic simulation parameters	
Sampling frequency	70 MHz
Sound speed	1540 m/s
Excitation signal	3-cycle sine at 7 MHz weighted by a Hamming window
Focal distance	25 mm
Central frequency	7 MHz
Aperture radius (r_{p})	6 mm (~30 λ)
Bandwidth (-6 dB)	72.6 %
Element size (squares)	200 µm
Number of elements (N_{e})	256
Elements apodization	None
Communication mechanism Θ	
Single translation (max)	±200 µm
Minimum kerf	λ/20
Measurement hemisphere radius	
N_{H}=1	25 mm
N_{H}=3	15, 25, 35 mm

The side- to main-lobe energy ratio (SMER) is defined as the log compressed ratio between the average intensity outside and inside the focal region, i.e., the region surrounding the focus delimited by the −6 dB isosurface.

The SLL was estimated as the log compressed ratio between the intensities of the highest secondary lobe and the main lobe.

The sensitivity was estimated as the ratio between the focus intensity and that resulted for the simulation of a 20 λ-radius spiral array having 0.5 λ-wide elements as used in [32].

The depth of field (DOF) is the −6 dB length along the steering direction.

The lateral resolution is computed as the average −6 dB width of the main beam (full-width at half-maximum) in a plane perpendicular to the US propagation direction.

The angle error measures the difference between the principal direction of the −6 dB isosurface angle and the set steering angle.

III. RESULTS: OPTIMIZED 2-D SPARSE ARRAYS AND SPIRAL ARRAY COMPARISON

A. Optimization Setup

In this paper, the state space Ω, the communication mechanism Θ, and the parameters listed in Table I were the same for all of the 16 performed optimizations. The targeted application was for peripheral vessel imaging, and Table I gives the aperture radius (6 mm = ~30λ), the central frequency (7 MHz), and the bandwidth (72%) of the considered arrays. The same element size (200 ≈ λ) of the reference spiral array was considered to improve the sensitivity of the sparse array probe. For the multidepth approach, N_{H} was set to three (Fig. 1) to check the performance before, after, and at focal

TABLE II
FINAL ENERGY FUNCTION VALUES FOR DIFFERENT N_{iter}

Array ID	Iter 640k	Iter 1.28M	Iter 1.92M	Iter 2.56M
σ	2500	5000	7500	10000
N_{iter}	640 000	1 280 000	1 920 000	2 560 000
U_1 ($\times 10^3$)	33.3	25.9	19.6	17.7

TABLE III
FINAL ENERGY FUNCTION VALUES ASSOCIATED WITH THE OPTIMIZATION RESULTS FOR DIFFERENT N_{PMP}

Array ID	PMPs 0.5k	PMPs 1k	PMPs 2k	PMPs 3k	PMPs 4k	PMPs 5k
N_{PMP}	500	1000	2000	3000	4000	5000
U_1 ($\times 10^3$)	74.7	36.5	22.1	11.8	35.1	25.9

depth. The choice of radius $R_1 = 15$ mm, $R_2 = 25$ mm, and $R_3 = 35$ mm (Table I) was motivated by the 25.3-mm DOF of the spiral array, i.e., the main beam pressure was expected to be still over -6 dB from 15- to 35-mm depths. According to Section II-A3b, for each depth R_1, R_2, and R_3, the main lobe width was set to $\theta_{\text{ML}}(R_1) = 13.7°$, $\theta_{\text{ML}}(R_2) = 5.5°$, and $\theta_{\text{ML}}(R_3) = 9.6°$, i.e., the -30 dB main lobe width of the spiral array at the respective depths. The performance of the spiral array [32] and those of the optimized 2-D sparse arrays were compared to evaluate how N_{iter}, N_{PMP}, N_{H}, and the expression of U impact on the final results, as detailed in the following.

B. Number of Iterations

N_{iter} influences the speed of the cooling sequence β_n, i.e., the greater is N_{iter} the slower is the temperature cooling down from $1/\beta_{\text{inf}}$ to $1/\beta_{\text{sup}}$. The optimization process always started from a 256-element initial sparse array (chosen randomly by activating only $N_e = 256$ elements of a full array with the same acoustic parameters as presented in Table I), which was optimized using $N_{\text{PMP}} = 5000$ on each of the $N_{\text{H}} = 3$ hemispheres (Table I) and U_1 as energy function expression. The effect of changing the number of iterations, $N_{\text{iter}} = \sigma K$, was tested by setting σ to 2500, 5000, 7500, and 10 000, while K was kept equal to 256. The associated values of U_1 are presented in Table II.

The final values of U_1 associated with optimal states (Table II) decrease when more iterations are done. This result confirms that the more the iterations, the higher the probability of reaching a global minimum [47]. As expected, the performance of the optimized arrays improved when increasing N_{iter}. In all the following experiments, N_{iter} was fixed to the maximum 2.56 M, unless otherwise stated.

C. Number of Pressure Measurement Points

The impact of the number of PMPs N_{PMP} on the final value of U_1 was assessed by optimizing the sparse array with $N_{\text{iter}} = 1.28$ M, $N_{\text{H}} = 3$, and $N_{\text{PMP}} = 500$, 1000, 2000, 3000, 4000, and 5000 (Table III). The configuration obtained when using 3000 PMPs (*PMPs 3k*) yields the lowest energy function value. Since it provides a good angular resolution sampling for the beam pattern analysis (15 PMPs per degree), N_{PMP} was set to 3000 for the following optimizations.

D. Number of Hemispheres

The impact of using multidepth energy functions with $N_{\text{H}} = 3$ measurement hemispheres is evaluated by comparing the optimized configurations obtained with the 1HS and 3HS versions of the energy functions U_1–U_3. The optimization setup of the multidepth approach is detailed in Section III-A. Fig. 3 shows the layouts of the optimized configurations with 1HS (U_1 1HS, U_2 1HS, U_3 1HS) and 3HS (U_1 3HS, U_2 3HS, U_3 3HS) and of the reference spiral array, while Fig. 4 shows the associated radiating patterns at 0° and 30° steering angles.[1]

Fig. 4 qualitatively highlights the benefits of using multidepth energy functions in both steered and notsteered cases. Indeed for the three definitions of U, at 15- and 35-mm depths, the 3HS profiles have much lower SLL than the 1HS profiles and this is also valid when the beam is steered by 30°. A quantitative analysis of the unsteered case can be done from Table IV(c) and (d) showing that the SLL at 15-mm depth of U_1 3HS, U_2 3HS, and U_3 3HS are 14.3, 12.3, and 13.6 dB lower than in the respective 1HS cases. Similarly, at 35-mm depth, the SLLs for 3HS cases are 10.6, 8.7, and 11.1 dB lower than for the respective 1HS. This denotes an uncontrolled behavior of the pressure field before and after the focal depth in the 1HS cases, and it clearly enlightens the performance improvement due to the multidepth approach. Moreover, even when no steering is done, the main lobes of the 1HS profiles are not centered around $\theta = 0°$ and the bias can reach up to 5° at depth $R_1 = 15$ mm. On the contrary, the 3HS profiles present a centered main lobe followed by a flat *plateau* up to $\theta = 40°$–$45°$.

However, analyzing Table IV(c) and (d) at the focal depth ($R_2 = 25$ mm), with respect to the 1HS versions, the 3HS versions increase, on average, by 1.0 dB and 0.8° the SLL and the -6 dB main lobe width, respectively. This indicates that, at the focal depth, for any expression of U, the 1HS version is slightly more efficient. A possible explanation could be that no compromises have to be done with the pressure behavior at other depths. In spite of the small performance improvement at the focal depth when using the single hemisphere approach, the uncontrolled behavior of the pressure field before and after the focal depth discards such solutions. This remark is corroborated by the 3-D performance analysis obtained over 81 steering angles: Fig. 5 and Table V(c) and (d) show that the 3-D performance clearly improves in terms of SLL, DOF (especially its limited deviation), sensitivity, and steering angles error while the resolution gets coarser when comparing 3HS and 1HS optimizations. For example, U_3 3HS compared with U_3 1HS yields 2.2-dB reduction of the median SLL, 11.4-mm DOF increase (+75%), 1.9-dB sensitivity increase,

[1]This paper has supplementary downloadable material available at http://ieeexplore.ieee.org, provided by the authors. This includes six videos illustrating the individual optimization run of the U_1 1HS, U_2 1HS, U_3 1HS, U_1 3HS, U_2 3HS, and U_3 3HS and a readme file. This material is 29 MB in size.

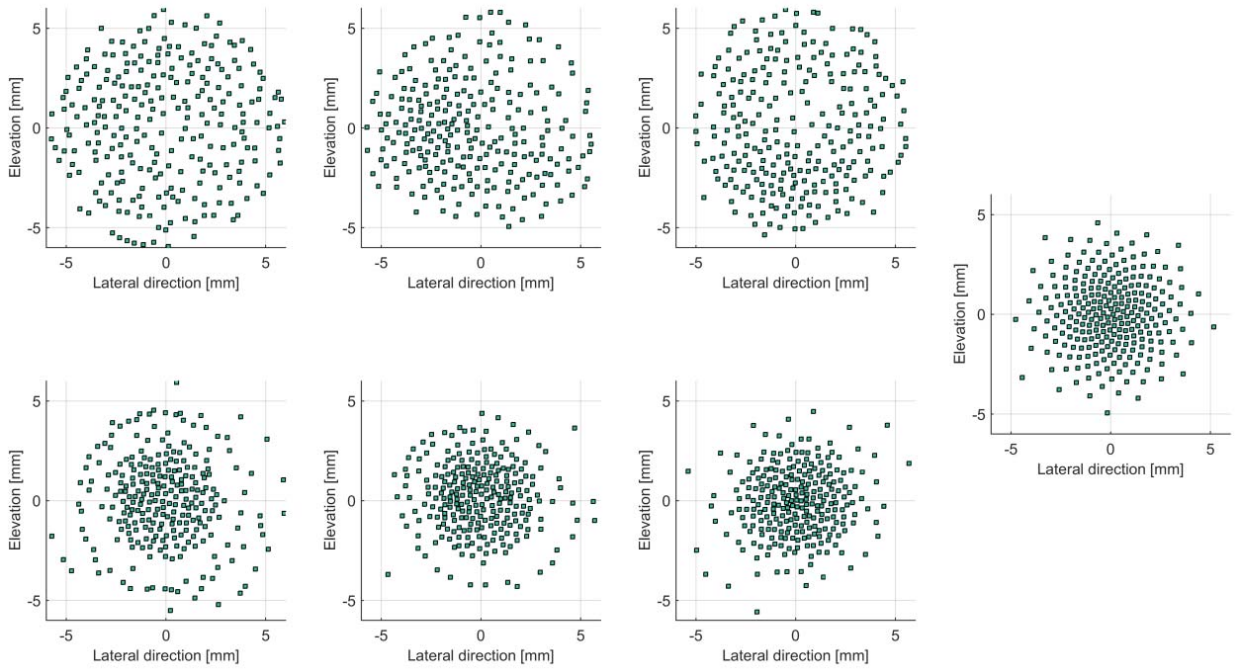

Fig. 3. Layouts of the optimization results when using one hemisphere (top, from left to right: U_1 1HS, U_2 1HS, and U_3 1HS) and when using three hemispheres (bottom, from left to right: U_1 3HS, U_2 3HS, and U_3 3 HS). The layout of the Blackman-tapered spiral array is also shown on the very right hand.

TABLE IV

FOR EACH OPTIMAL ARRAY WE PRESENT THE OBTAINED SLL AND MAIN LOBE WIDTH ON THE THREE HEMISPHERES OF RADIUS 15, 25, AND 35 mm

	Optimization Setup					Side Lobe Level (in dB)			Main Lobe Width at -6dB (in degree)		
	Array ID	N_{iter}	N_{PMP} (per HS)	N_{H}	U	15mm	25 mm	35 mm	15mm	25 mm	35 mm
a	Iter 640 k	0.64 M	5k	3	U_1	-20.1	-24.4	-19.8	3.0	1.9	4.2
	Iter 1.28M	1.28 M	5k	3	U_1	-20.0	-24.8	-22.6	3.9	2.1	2.4
	Iter 1.92M	1.92 M	5k	3	U_1	-21.1	-26.0	-23.5	4.0	2.1	3.9
	Iter 2.56M	2.56 M	5k	3	U_1	-21.4	-24.9	-24.1	6.7	2.2	3.9
b	PMPs 0.5k	1.28 M	0.5k	3	U_1	-17.4	-23.5	-17.5	5.1	2.0	4.3
	PMPs 1k	1.28 M	1k	3	U_1	-19.5	-26.3	-19.8	3.0	2.1	4.5
	PMPs 2k	1.28 M	2k	3	U_1	-20.3	-25.1	-22.9	7.5	2.1	4.2
	PMPs 3k	1.28 M	3k	3	U_1	-22.3	-26.4	-24.4	5.4	2.0	4.0
	PMPs 4k	1.28 M	4k	3	U_1	-19.5	-24.6	-24.1	4.2	2.1	3.4
	PMPs 5k	1.28 M	5k	3	U_1	-20.0	-24.8	-22.6	3.9	2.1	2.4
c	U_1 1HS	2.56 M	3k	1	U_1	-9.4	-28.9	-14.7	14.1	1.6	6.1
	U_2 1HS	2.56 M	3k	1	U_2	-12.1	-29.3	-18.8	8.3	1.9	6.0
	U_3 1HS	2.56 M	3k	1	U_3	-10.9	-29.3	-16.5	12.2	1.6	6.6
d	U_1 3HS	2.56 M	3k	3	U_1	-23.7	-27.5	-25.3	4.6	2.2	3.8
	U_2 3HS	2.56 M	3k	3	U_2	-24.4	-27.4	-27.5	5.3	2.7	3.7
	U_3 3HS	2.56 M	3k	3	U_3	-24.5	-29.7	-27.6	6.1	2.6	3.4
	Spiral	-	-	-	-	-20.2	-29.3	-25.2	7.8	2.6	3.8

1.1° angle error reduction (−65%), and 0.4-mm worse resolution (5% coarser than the spiral, see Table V). The same trend is observed with U_1 and U_2. It is worth noting that the multidepth energy functions (3HS) strongly improve the steering angle precision (9% better than the spiral array for U_3 3HS; see Table V); hence, the proposed approach not only controls the focal point to be accurate but also leads the beam direction to be aligned with the desired steering angle.

In conclusion, the multidepth energy function approach improves the array performance in terms of SLL, DOF, sensitivity, and angle error even in steering condition and independently from the energy function expression. Although a tradeoff is done on the resolution (at focal depth), a more regular shape of the main lobe close to the array and a better alignment between the beam direction and the steering angle are obtained.

E. Energy Function

The performances of the three optimized layouts U_1 3HS, U_2 3HS, and U_3 3HS and of the reference spiral array were evaluated. A qualitative comparison of the profiles shown in Fig. 4 highlights that the energy function U_1 3HS leads to slightly higher SLL with respect to U_2 3HS and U_3 3HS, in

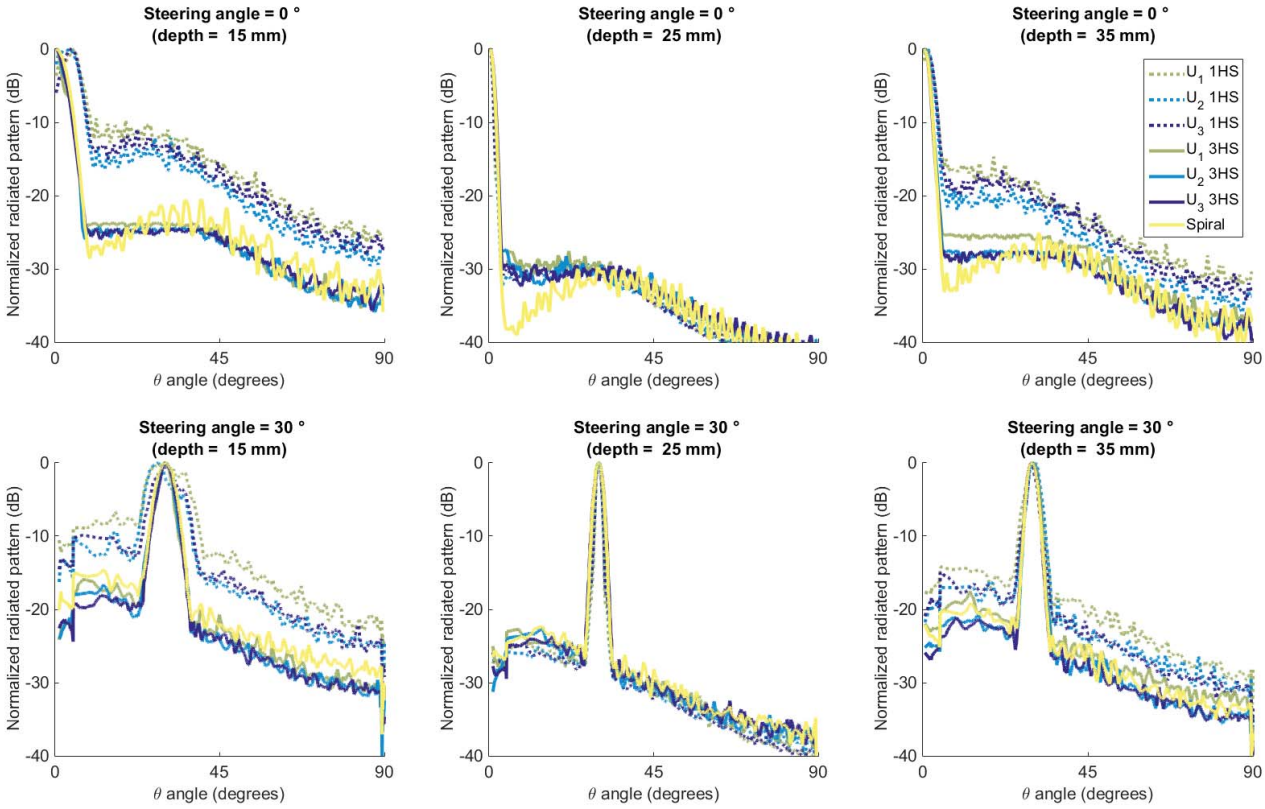

Fig. 4. Radiated patterns at depths 15 (left), 25 (center), and 35 mm (right) of the optimization results and the spiral array. The steering angles were 0° (top) and 30° (bottom).

TABLE V

MEDIAN VALUES OF THE RESULTS PRESENTED IN FIG. 5. THE 3-D PERFORMANCE METRICS WERE EVALUATED OVER 81 STEERING ANGLES

	Array ID	SLL (in dB)	Resolution (mm)	DOF (mm)	SMER (dB)	Sensitivity (dB)	Steering angle error (°)
a	Iter 640 k	-14.2	1.2	20.5	-27.9	8.1	0.9
	Iter 1.28M	-15.1	1.2	20.9	-27.9	8.2	1.3
	Iter 1.92M	-15.6	1.3	21.8	-28.2	8.5	0.9
	Iter 2.56M	-15.2	1.3	23.1	-28.3	8.7	1.3
b	PMPs 0.5k	-15.4	1.2	20.6	-28.0	8.2	1.3
	PMPs 1k	-14.9	1.2	20.9	-28.6	8.2	1.4
	PMPs 2k	-15.3	1.3	21.5	-28.6	8.4	1.4
	PMPs 3k	-15.5	1.3	22.0	-28.7	8.4	0.9
	PMPs 4k	-15.4	1.3	22.4	-28.5	8.4	2.2
	PMPs 5k	-15.1	1.2	20.9	-27.9	8.2	1.3
c	U_1 1HS	-14.2	1.1	12.9	-28.0	7.3	2.0
	U_2 1HS	-15.2	1.2	16.8	-28.1	7.8	3.0
	U_3 1HS	-14.3	1.1	15.2	-28.7	7.6	1.8
d	U_1 3HS	-15.6	1.3	23.0	-29.0	8.8	0.9
	U_2 3HS	-16.5	1.5	25.8	-28.8	9.3	0.9
	U_3 3HS	-16.5	1.5	26.6	-28.8	9.5	0.6
	Spiral	-15.6	1.4	25.3	-28.8	9.5	0.7

both steered and unsteered cases. It can be observed that the spiral array presents a deeper trough at the bottom of the main lobe but also higher SLL than the three optimized results. More quantitatively, Table V(d) shows that U_1 3HS reaches the best resolution median (1.3 mm), but is not as close as U_2 3HS and U_3 3HS to the spiral arrays performance on the other criteria. Compared with the spiral array, U_2 3HS tends to improve the SLL (−0.9 dB) and reaches very similar results in terms of sensitivity (−0.2 dB), SMER (+0.0 dB), and DOF (+0.5 mm), while the resolution is getting slightly worse (+0.1 mm) and the angle error is increased by 0.2°. U_3 3HS is very competitive on SLL (−0.9 dB), DOF (+1.3 mm), SMER (+0.0 dB), sensitivity (+0.0 dB), and angle error (−0.1°), but the resolution is a little coarser (+0.1 mm). Fig. 6 helps to conduct an overall comparison among the 3HS optimized arrays and the spiral array. Fig. 6 represents the array performance with the worst case of each parameter close to the center of the radar plot and the best performance on the external Web line.

To summarize, it may be concluded that the U_1 energy function, by its definition, tries to push down the SLL only once the main lobe is thinner than expected. Indeed until the

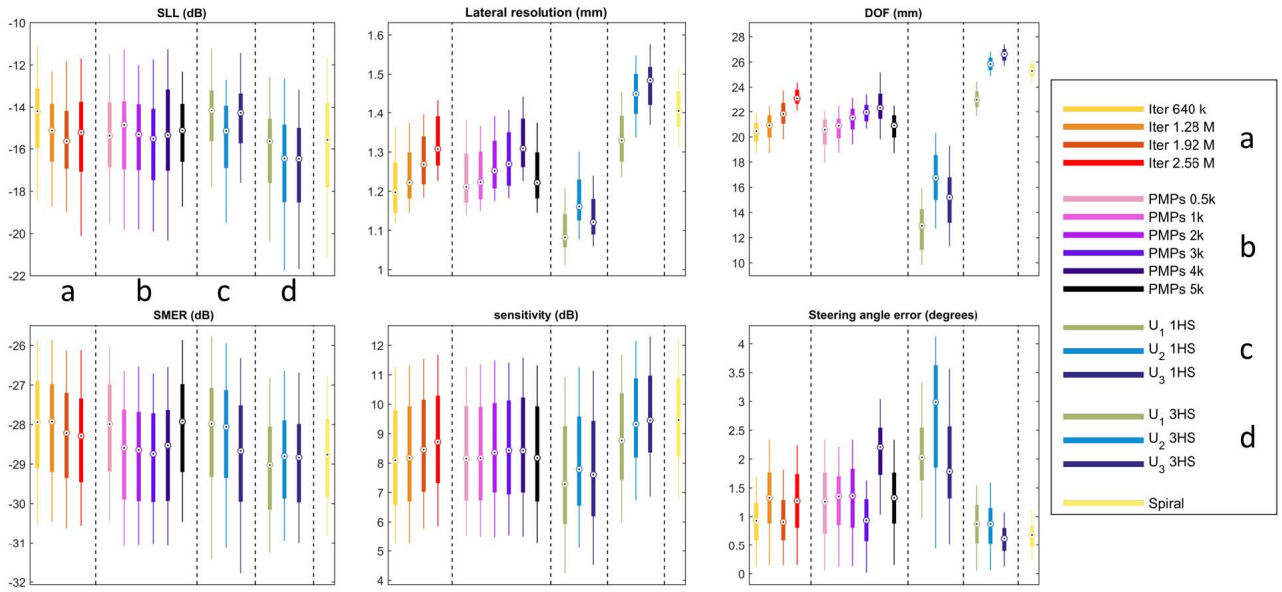

Fig. 5. SLL, Lateral resolution, DOF, SMER, sensitivity, and steering angle error from the 3-D pressure field analysis (statistics over 81 steering angles for each array). Simulations were done in a $40 \times 40 \times 30$ mm^3 volume starting at $z = 10$ mm over the arrays.

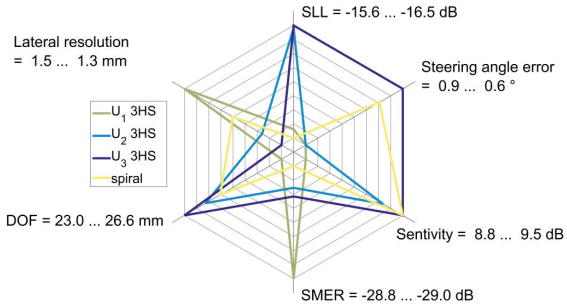

Fig. 6. Radar plot comparison for U_1 3HS, U_2 3HS, U_3 3HS, and the spiral array.

entire main lobe gets inside the delimited main lobe region L, the outstripping part is considered as a lateral lobe with very high level compared with the real side lobes. Since the resolution constraint has priority on the contrast constraint, the U_1 energy function is not likely to balance the tradeoff between them. The U_2 expression starts to better integrate the tradeoff thanks to the pressure ratio that implies both an SLL reduction and a concentration of the acoustic energy in the main lobe. Major improvements are reached by U_3 because it also sculpts the main lobe shape.

IV. Discussion

Two-dimensional sparse array probes were so far designed by optimizing the pressure field at only one distance from the probe center. The proposed method, including acoustic simulations and multidepth energy functions, represents a first step toward the 3-D optimization of the pressure field around the probe. The simulation results also suggest that great care should be taken in the definition of the optimization mask, which, in turn, depends on the targeted application.

TABLE VI

Barycenter Bias of the 256 Elements for Each Optimization Results Shown in Fig. 3

	1HS			3HS			Spiral
	U_1	U_2	U_3	U_1	U_2	U_3	
Barycenter bias (λ)	0.8	2.0	0.3	0.1	0.8	0.4	0.1

The proposed method also raises specific aspects about the transducer design that are discussed in the following.

A. Layout Characteristics

The results in Fig. 3 show that the elements are significantly concentrated in the center of the aperture when the multidepth (3HS), rather than the single-depth (1HS), energy functions are used. In the case of U_3 3HS, they are even more concentrated in the center than in the spiral array. In the 1HS cases, the highest density region appears to be eccentric. However, the bias of the element position barycenter is low ($<\lambda$) in most of the cases and it is further reduced with the multidepth energy functions (see Table VI). A bias of the highest density region, for instance, with U_2 1HS, may strongly increase the steering angle error (Fig. 5 and Table V).

In most previous optimization studies, a circular symmetry was assumed as a prerequisite to guarantee the same performance for any ϕ angle (i.e., there should be no effect on the image quality if the probe is rotated around the z-axis). A further advantage of assuming the symmetry is the state space reduction, which favors a faster convergence of the algorithm. Even though in our method the elements can arbitrarily move over the aperture, the multidepth approach yields a circular symmetry without any *a priori* constraint. Moreover, in both U_1 3HS and U_2 3HS and, at a minor extent in U_3 3HS, an annular array may be observed around

the central dense cluster. Usually, the resolution is linked to the size of the array and the lateral lobes are related to the sampling of the aperture surface. In this geometry, the annular array widens the size of the array and contributes to improve the resolution performance; while the central cluster contributes to reduce the GLL by the aperiodic space sampling and reduce the SLL by the density tapering. This hypothesis will be further investigated.

In this paper, the position of the elements is the only degree of freedom taken into consideration. Even though other variables could have been considered, such as the use of elements with variable size, the chosen strategy fits well with current fabrication processes like laser cutting [51] and micromachining techniques [52], and no variable impedance matching is needed. This choice is further supported by the strong improvements observed in nongrid sparse arrays in terms of radiated beam pattern [35] and by density tapering in terms of SLL and sensitivity [32], [53].

The element size is important since it impacts the field of view: the wider the elements, the weaker the steering capability of the array. Here, the choice of an element size close to λ aimed at compensating for the sensitivity lack of sparse arrays by increasing the active surface. Yet, the optimized arrays yield good performance over a wide field of view (FOV) ($-32°$; $+32°$).

B. Degrees of Freedom and Constraints

The fast pressure field update [45] allows moving the elements out of grid during the optimization without continuous wave approximation. Moreover, the wideband acoustic simulations suggest exploring new degrees of freedom while considering more realistic constraints. Indeed, the effects of the excitation signal, the impulse response, and the element orientation and size could be taken into account. Furthermore, the proposed approach could permit possible geometrical constraints (e.g., the presence of "keep-out" areas on the probe surface or curved aperture surface) to be included in the state space. Integrating special geometrical constraints could not be obvious designing the array with a deterministic analytical equation. This raises the possible interest of optimizing the probe layout under geometrical constraints required by the application or some accessibility hardships that could influence the general shape of the array.

C. Multidepth Energy Function

The introduction of the new energy function that shapes the beam pattern at several depths represents a first step toward a 3-D control of the pressure field. Indeed, the multidepth energy function shows how the quality of the transmitted beam can be shaped along the propagation direction. The multidepth approach yields a strong reduction of the angle error when using 3HS (compared with 1HS, see Section III-D), which is important to avoid artifacts implied from the misalignment between the desired steering angle and the direction of the beam. Moreover, even if a reflector in the side lobe region at depth R_1 (or R_3) is time separated from a pixel reconstructed at depth R_2, it is worth having low side lobes at depths R_2 and R_1 (or R_3) if the same transmission is used to reconstruct pixels located at both depths. As a potential perspective, the multidepth energy functions could be adapted for HIFU and dual-mode transducers where the minimization of the spread energy outside of the target located at focal point (for instance, by minimizing the pressure intensity at depth R_1 and R_3 compared with focal depth R_2) is critical to preserve safe tissues. Probably that other imaging sequences such as plane or diverging waves strategies could take advantage of the multidepth energy functions, for instance, by optimizing the array to have the beam pattern as homogeneous as possible at each depths. Further studies would be required to demonstrate the suggested perspectives.

How choosing a tradeoff among resolution, contrast, and depth-of-field depends, in general, on the application. In particular, in our experiments, the layout was optimized for peripheral vascular applications. For these applications, the deterministic approach presented in [32] yields satisfying performance with ultralight computation load. The Blackman-tapered spiral array configuration was thus chosen as the reference to validate our approach. Actually, the proposed energy functions (in particular U_3) were directly inspired by the reference spiral array and the resulting constraints directly fit with its radiated beam pattern, as detailed in Section II-A3b. The energy function design could be further developed to influence the tradeoff into a desired direction. For instance, in the presented multidepth approach, a different weight could be applied to each hemisphere, e.g., by giving more weight to the central hemisphere to favor the resolution at the expenses of DOF and image contrast. The distance between the hemispheres and their number could also be increased to optimize specific depths or to extend the DOF. Eventually, an effective 3-D sculpt of the pressure field during the optimization process could be included, however, with a significant increase in the computation load. A more powerful hardware, exploiting a GPU implementation of our method, would enable the extension to 3-D-energy functions including 3-D performance metrics (see Section II-C1).

D. Optimization Setup

As observed in Section III-B, the probability of reaching a global minimum increases with the number of iterations N_{iter}, as confirmed by the evolution of the energy function in Table II. Moreover, Table IV(a) shows that when N_{iter} increases from 0.64 to 2.56 M, the SLL decreases from -20.1 to -21.4 dB and from -19.8 to -24.1 dB at depths of 15 and 35 mm, respectively. However, *Iter 1.92M* array is an exception: it yielded the lowest SLL over the 25-mm hemisphere (Table IV) and the best median SLL value [Table V(a)]. In spite of this isolated result, it is highly recommended to run as many iterations as possible since it increases the probability of reaching a lower minimum of the global energy (Table II).

The influence of the number of PMPs analyzed in Section III-C [Table IV(b)] has highlighted the related serious impact: the SLL obtained with *PMPs 3k* was 4.9, 2.9, and 6.9 dB lower than *PMPs 0.5k* at depths 15, 25, and 35 mm, respectively. The peaks of the radiated pattern are more

likely to be missed at low resolution. However, according to Table IV(b), *PMPs 3k* yields better results in terms of SLL than *PMPs 5k*. Indeed, the SLL of *PMPs 3k* were 2.3, 1.6, and 1.8 dB lower than for *PMPs 5k* at depths 15, 25, and 35 mm, respectively. Moreover, in Table V(b), the results obtained with *PMPs 3k* on the 3-D simulations of 81 steering angles were slightly better than with *PMPs 5k* in terms of SLL (-0.4 dB), DOF ($+1$ mm), ER (-0.8 dB), sensitivity ($+0.3$ dB), and angle error ($-0.4°$). Because it makes the energy topology more difficult, increasing N_{PMP} should be accompanied by an increase in N_{iter} to hope for a similar performance. This may explain why, when performing the same number of iterations, better results are obtained with $N_{\text{PMP}} = 3000$ rather than with $N_{\text{PMP}} = 5000$ in Section III-C.

V. Conclusion

In this paper, the integration of acoustic simulations in the SA optimization process enabled the definition of multidepth energy functions that take into account the pressure field behavior at different depths. Moreover, thanks to the acoustic simulation, a wideband excitation signal, the pulse response, and the size of the elements were taken into account during the optimization process. The effects of changing the number of iterations, the number of PMPs, the number of hemispheres, and the energy function definition were studied. Three different energy functions inspired by the Blackman-tapered spiral array (here chosen as reference) were defined, and their performance was compared. Sixteen optimized arrays were analyzed in terms of lateral lobes level, resolution, sensitivity, SMER, DOF, and steering angle error. The comparison criteria were based on performance metrics evaluated on 3-D pressure field simulations at 81 steering angles (from $-32°$ to $+32°$) for each array. An optimized array provided results slightly better than the reference spiral array and illustrated that sculpting the main beam shape at several depths leads to a circular symmetry of the layouts without imposing any geometrical constraint. Further work is necessary to explore solutions with more degrees of freedom (e.g., elements' shapes and size). Future investigations will also concern multiscale approaches with stochastic continuation where the energy function can evolve during the optimization process.

References

[1] E. R. Pospisil, R. Rohling, R. Z. Azar, and S. E. Salcudean, "4-D × 3-D ultrasound: Real-time scan conversion, filtering, and display of displacement vectors with a motorized curvilinear transducer," *IEEE Trans. Ultrason., Ferroelect., Freq. Control*, vol. 57, no. 10, pp. 2271–2283, Oct. 2010.

[2] H. Andresen, "Three-dimensional ultrasound imaging using a rotating array," Dept. Electron. Signal Process., Tech. Univ. Denmark, Kongens Lyngby, Denmark, Tech. Rep. 193125, 2006.

[3] S. I. Nikolov, J. A. Jensen, L. Dufait, and A. Schoisswohl, "Three-dimensional real-time synthetic aperture imaging using a rotating phased array transducer," in *Proc. IEEE Ultrason. Symp.*, vol. 2. Oct. 2002, pp. 1585–1588.

[4] B. Savord and R. Solomon, "Fully sampled matrix transducer for real time 3D ultrasonic imaging," in *Proc. IEEE Symp. Ultrason.*, vol. 1. Oct. 2003, pp. 945–953.

[5] W. F. Walker *et al.*, "The sonic window: Second generation results," *Proc. SPIE*, vol. 6147, pp. 61470B-1–61470B-7, Mar. 2006.

[6] J. M. Abeysekera, M. Najafi, R. Rohling, and S. E. Salcudean, "Calibration for position tracking of swept motor 3-D ultrasound," *Ultrasound Med. Biol.*, vol. 40, no. 6, pp. 1356–1371, Jun. 2014.

[7] J. Provost *et al.*, "3D ultrafast ultrasound imaging *in vivo*," *Phys. Med. Biol.*, vol. 59, no. 19, p. L1, Oct. 2014.

[8] J. L. Gennisson *et al.*, "4-D ultrafast shear-wave imaging," *IEEE Trans. Ultrason., Ferroelect., Freq. Control*, vol. 62, no. 6, pp. 1059–1065, Jun. 2015.

[9] J.-F. Deprez, E. Brusseau, C. Schmitt, G. Cloutier, and O. Basset, "3D estimation of soft biological tissue deformation from radio-frequency ultrasound volume acquisitions," *Med. Image Anal.*, vol. 13, no. 1, pp. 116–127, Feb. 2009.

[10] T. Deffieux, J. L. Gennisson, M. Tanter, and M. Fink, "Assessment of the mechanical properties of the musculoskeletal system using 2-D and 3-D very high frame rate ultrasound," *IEEE Trans. Ultrason., Ferroelect., Freq. Control*, vol. 55, no. 10, pp. 2177–2190, Oct. 2008.

[11] L. Sugeng *et al.*, "Quantitative assessment of left ventricular size and function: Side-by-side comparison of real-time three-dimensional echocardiography and computed tomography with magnetic resonance reference," *Circulation*, vol. 114, no. 7, pp. 654–661, Aug. 2006.

[12] Y. Zhao, A. Bernard, C. Cachard, and H. Liebgott, "Biopsy needle localization and tracking using ROI-RK method," *Abstract Appl. Anal.*, vol. 2014, Oct. 2014, Art. no. 973147.

[13] C. Nadeau, H. Ren, A. Krupa, and P. Dupont, "Intensity-based visual servoing for instrument and tissue tracking in 3D ultrasound volumes," *IEEE Trans. Autom. Sci. Eng.*, vol. 12, no. 1, pp. 367–371, Jan. 2015.

[14] G. Unsgaard *et al.*, "Intra-operative 3D ultrasound in neurosurgery," *Acta Neurochirurgica*, vol. 148, no. 3, pp. 235–253, Dec. 2005.

[15] F. Lindseth *et al.*, *Ultrasound-Based Guidance and Therapy, Advancements and Breakthroughs in Ultrasound Imaging*, G. P. P. Gunarathne, Ed. Rijeka, Croatia: InTech, 2013. [Online]. Available: http://www.intechopen.com/books/advancements-and-breakthroughs-in-ultrasound-imaging/ultrasound-based-guidance-and-therapy, doi: 10.5772/55884.

[16] S. W. Smith, H. G. Pavy, Jr., and O. T. von Ramm, "High-speed ultrasound volumetric imaging system—Part I: Transducer design and beam steering," *IEEE Trans. Ultrason., Ferroelect., Freq. Control*, vol. 38, no. 2, pp. 100–108, Mar. 1991.

[17] E. D. Light, S. F. Idriss, P. D. Wolf, and S. W. Smith, "Real-time three-dimensional intracardiac echocardiography," *Ultrasound Med. Biol.*, vol. 27, no. 9, pp. 1177–1183, Sep. 2001.

[18] M. F. Rasmussen and J. A. Jensen, "3-D ultrasound imaging performance of a row-column addressed 2-D array transducer: A measurement study," in *Proc. IEEE Int. Ultrason. Symp. (IUS)*, Jul. 2013, pp. 1460–1463.

[19] T. L. Christiansen, M. F. Rasmussen, J. P. Bagge, L. N. Moesner, J. A. Jensen, and E. V. Thomsen, "3-D imaging using row–column-addressed arrays with integrated apodization—Part II: Transducer fabrication and experimental results," *IEEE Trans. Ultrason., Ferroelect., Freq. Control*, vol. 62, no. 5, pp. 959–971, May 2015.

[20] J. Kortbek, J. A. Jensen, and K. L. Gammelmark, "Sequential beamforming for synthetic aperture imaging," *Ultrasonics*, vol. 53, no. 1, pp. 1–16, Jan. 2013.

[21] G. Matrone, A. S. Savoia, M. Terenzi, G. Caliano, F. Quaglia, and G. Magenes, "A volumetric CMUT-based ultrasound imaging system simulator with integrated reception and μ-beamforming electronics models," *IEEE Trans. Ultrason., Ferroelect., Freq. Control*, vol. 61, no. 5, pp. 792–804, May 2014.

[22] R. Fisher *et al.*, "Reconfigurable arrays for portable ultrasound," in *Proc. IEEE Ultrason. Symp.*, vol. 1. Sep. 2005, pp. 495–499.

[23] I. O. Wygant *et al.*, "An integrated circuit with transmit beamforming flip-chip bonded to a 2-D CMUT array for 3-D ultrasound imaging," *IEEE Trans. Ultrason., Ferroelect., Freq. Control*, vol. 56, no. 10, pp. 2145–2156, Oct. 2009.

[24] K. Chen, "A column-row-parallel ASIC architecture for 3D wearable/portable medical ultrasonic imaging," M.S. thesis, Dept. Elect. Eng. Comput. Sci., Massachusetts Inst. Technol., Cambridge, MA, USA, 2014.

[25] A. S. Logan, L. L. P. Wong, A. I. H. Chen, and J. T. W. Yeow, "A 32 × 32 element row-column addressed capacitive micromachined ultrasonic transducer," *IEEE Trans. Ultrason., Ferroelect., Freq. Control*, vol. 58, no. 6, pp. 1266–1271, Jun. 2011.

[26] A. L. Robinson, D. N. Roundhill, B. S. Robinson, and P. Detmer, "2D ultrasonic transducer array for two dimensional and three dimensional imaging," U.S. Patent 6 582 367 B1, Jun. 24, 2003.

[27] K. E. Thomenius, R. G. Wodnicki, and Y.-M. Li, "Transmit and receive interface array for highly integrated ultrasound scanner," U.S. Patent 7 775 979 B2, Aug. 17, 2010.

[28] S. Barnes, M. Bolorforosh, and R. Phelps, "System and method for 2D partial beamforming arrays with configurable sub-array elements," U.S. Patent 2005 0 228 277 A1, Oct. 13, 2005.

[29] S. S. Brunke and G. R. Lockwood, "Broad-bandwidth radiation patterns of sparse two-dimensional vernier arrays," *IEEE Trans. Ultrason., Ferroelect., Freq. Control*, vol. 44, no. 5, pp. 1101–1109, Sep. 1997.
[30] A. Austeng and S. Holm, "Sparse 2-D arrays for 3-D phased array imaging—Design methods," *IEEE Trans. Ultrason., Ferroelect., Freq. Control*, vol. 49, no. 8, pp. 1073–1086, Aug. 2002.
[31] O. Martínez-Graullera, C. J. Martín, G. Godoy, and L. G. Ullate, "2D array design based on Fermat spiral for ultrasound imaging," *Ultrasonics*, vol. 50, no. 2, pp. 280–289, Feb. 2010.
[32] A. Ramalli, E. Boni, A. S. Savoia, and P. Tortoli, "Density-tapered spiral arrays for ultrasound 3-D imaging," *IEEE Trans. Ultrason., Ferroelect., Freq. Control*, vol. 62, no. 8, pp. 1580–1588, Aug. 2015.
[33] B. V. Ha, R. E. Zich, M. Mussetta, and P. Pirinoli, "Thinned array optimization by means of M-cGA," in *Proc. IEEE Antennas Propag. Soc. Int. Symp. (APSURSI)*, Jul. 2014, pp. 1956–1957.
[34] R. L. Haupt, "Thinned arrays using genetic algorithms," *IEEE Trans. Antennas Propag.*, vol. 42, no. 7, pp. 993–999, Jul. 1994.
[35] B. Diarra, M. Robini, P. Tortoli, C. Cachard, and H. Liebgott, "Design of optimal 2-D nongrid sparse arrays for medical ultrasound," *IEEE Trans. Biomed. Eng.*, vol. 60, no. 11, pp. 3093–3102, Nov. 2013.
[36] C. Sciallero and A. Trucco, "Design of a sparse planar array for optimized 3D medical ultrasound imaging," presented at the 23rd Eur. Signal Process. Conf. (EUSIPCO), Nice, France, 2015.
[37] P. Chen, B.-J. Shen, L.-S. Zhou, and Y.-W. Chen, "Optimized simulated annealing algorithm for thinning and weighting large planar arrays," *J. Zhejiang Univ. Sci. C*, vol. 11, no. 4, pp. 261–269, Apr. 2010.
[38] A. Trucco, "Thinning and weighting of large planar arrays by simulated annealing," *IEEE Trans. Ultrason., Ferroelect., Freq. Control*, vol. 46, no. 2, pp. 347–355, Mar. 1999.
[39] A. Austeng, S. Holm, P. K. Weber, N. Aakvaag, and K. Iranpour, "1D and 2D algorithmically optimized sparse arrays," in *Proc. IEEE Ultrason. Symp.*, vol. 2. Oct. 1997, pp. 1683–1686.
[40] S. Holm and B. Elgetun, "Optimization of the beampattern of 2D sparse arrays by weighting," in *Proc. IEEE Ultrason. Symp.*, vol. 2. Nov. 1995, pp. 1345–1348.
[41] P. K. Weber, R. M. Schmitt, B. D. Tylkowski, and J. Steck, "Optimization of random sparse 2-D transducer arrays for 3-D electronic beam steering and focusing," in *Proc. IEEE Ultrason. Symp.*, vol. 3. Oct./Nov. 1994, pp. 1503–1506.
[42] J. W. Choe, O. Oralkan, and P. T. Khuri-Yakub, "Design optimization for a 2-D sparse transducer array for 3-D ultrasound imaging," in *Proc. IEEE Ultrason. Symp. (IUS)*, Oct. 2010, pp. 1928–1931.
[43] J. A. Jensen and N. B. Svendsen, "Calculation of pressure fields from arbitrarily shaped, apodized, and excited ultrasound transducers," *IEEE Trans. Ultrason., Ferroelect., Freq. Control*, vol. 39, no. 2, pp. 262–267, Mar. 1992.
[44] J. A. Jensen, "Field: A program for simulating ultrasound systems," *Med. Biol. Eng. Comput.*, vol. 34, no. 1, pp. 351–353, 1996.
[45] E. Roux, A. Ramalli, P. Tortoli, C. Cachard, M. Robini, and H. Liebgott, "Speed-up of acoustic simulation techniques for 2D sparse array optimization by simulated annealing," in *Proc. IEEE Int. Ultrason. Symp. (IUS)*, Oct. 2015, pp. 1–4.
[46] S. Kirkpatrick, C. D. Gelatt, and M. P. Vecchi, "Optimization by simulated annealing," *Science*, vol. 220, no. 4598, pp. 671–680, 1983.
[47] P. J. M. van Laarhoven and E. H. L. Aarts, "Simulated annealing," in *Simulated Annealing: Theory and Applications*. The Netherlands: Springer, 1987, pp. 7–15.
[48] M. C. Robini and P.-J. Reissman, "From simulated annealing to stochastic continuation: A new trend in combinatorial optimization," *J. Global Optim.*, vol. 56, no. 1, pp. 185–215, May 2013.
[49] M. C. Robini, "Theoretically grounded acceleration techniques for simulated annealing," in *Handbook of Optimization*, I. Zelinka, V. Snášel, A. Abraham, Eds. Heidelberg, Germany: Springer, 2013, pp. 311–335.
[50] N. Felix, M. Lethiecq, C. Millar, and L. P. Tran-Huu-Hue, "Influence of piezoceramic composition, pitch, and layout on the performances of sparse 2D array transducers for medical imaging," *Proc. SPIE*, vol. 3982, pp. 225–233, Apr. 2000.
[51] H. J. Vos *et al.*, "Transducer for harmonic intravascular ultrasound imaging," *IEEE Trans. Ultrason., Ferroelect., Freq. Control*, vol. 52, no. 12, pp. 2418–2422, Dec. 2005.
[52] C. Liu, F. T. Djuth, Q. Zhou, and K. K. Shung, "Micromachining techniques in developing high-frequency piezoelectric composite ultrasonic array transducers," *IEEE Trans. Ultrason., Ferroelect., Freq. Control*, vol. 60, no. 12, pp. 2615–2625, Dec. 2013.
[53] A. Ramalli and P. Tortoli, "256-element density-tapered spiral matrices for ultrasound phased imaging," in *Proc. IEEE Int. Ultrason. Symp. (IUS)*, Sep. 2014, pp. 2087–2090.

Emmanuel Roux (S'14) was born in Firminy, France, in 1990. He received the Electrical and Electronics Engineering degree in Master of Science (M.S.) and the M.Sc. degree in science for technologies and health from Lyon National Institute of Applied Sciences (INSA-Lyon), in 2013. He is currently a co-supervised Ph.D. candidate in acoustics and information engineering with both the University of Lyon, Lyon, France, and the University of Florence, Florence, Italy.

He teaches Applied Mathematics in the Electrical Engineering Department, the Technical Institute of Université Claude Bernard Lyon 1. His current research focuses on the 2-D transducer optimization for 3-D ultrasound Imaging. He is particularly interested in 3-D acoustics, stochastic optimization, and information processing for the health and entertainment sectors.

Alessandro Ramalli (S'10–M'12) was born in Prato, Italy, in 1983. He received the Electronics Engineering degree from the University of Florence, in 2008. In 2012, he received the Ph.D. degree in electronics system engineering from the University of Florence and in automatics, systems and images from the University of Lyon, by defending a thesis on the development of novel ultrasound techniques for imaging and elastography.

He currently holds a postdoctoral position with the MSD Laboratory, University of Florence, where he is involved in the development of the imaging section of a programmable open ultrasound system. His research interests include medical imaging, ultrasound simulation, and elastography.

Piero Tortoli (M'91–SM'96) received the Laurea degree in electronics engineering from the University of Florence, Florence, Italy, in 1978.

Since 1978, he has been on the faculty of the Electronics and Telecommunications (now Information Engineering) Department of the University of Florence, where he is currently full Professor of Electronics, leading a group of over 10 researchers in the Microelectronics Systems Design Laboratory. He has served on the IEEE International Ultrasonics Symposium Technical Program Committee since 1999, and is currently an Associate Editor of the IEEE TRANSACTIONS ON ULTRASONICS, FERROELECTRICS, AND FREQUENCY CONTROL. He chaired the 22nd International Symposium on Acoustical Imaging in 1995, the 12th New England Doppler Conference in 2003, and established the Artimino Conference on Medical Ultrasound in 2011. His research activity is centered on the development of ultrasound research systems and novel imaging/Doppler methods, on which he has authored more than 200 papers.

Prof. Tortoli was named an Honorary Member of the Polish Academy of Sciences in 2000.

Christian Cachard received the Ph.D. degree in acoustics from INSA-Lyon in 1988 in the field of signal processing for underwater acoustics.

He is now a Professor with the Electrical Engineering Department, the Technical Institute of Université Claude Bernard Lyon 1. Since he joined the research laboratory CREATIS, his domain of interest includes ultrasound medical imaging, ultrasound contrast agent imaging, ultrasound radio frequency processing, microtools localization in 3-D ultrasound data, and 2-D matrix arrays for 3-D imaging. He is a coauthor in 38 papers in peer-reviewed journals and has supervised 18 Ph.D. students.

Marc C. Robini received the M.Sc. degree in electrical and computer engineering and the Ph.D. degree in signal and image processing from the INSA-Lyon Engineering University, Lyon, France, in 1993 and 1998, respectively.

In 1999, he joined INSA-Lyon, where he is currently an Associate Professor of Mathematics and a Research Associate with the Center for Research and Applications in Image and Signal Processing (CREATIS), Lyon, France, CNRS Research Unit UMR5220, Paris, France, and INSERM Research Unit U1206, Paris. His current research interests include deterministic and stochastic optimization methods for large-scale inverse problems.

Hervé Liebgott (S'03–A'05) was born in France, in 1979. He received the Ph.D. degree from the Lyon National Institute of Applied Sciences (INSA Lyon), France, in 2005, and the French Habilitation to lead research (Hdr) degree, in 2011.

He is currently an Associate Professor with the Department of Electrical Engineering, University Institute of Technology, Lyon (GEII), and is also doing his research at Center for Research and Applications in Image and Signal Processing (CREATIS), Lyon, France, where he is currently the Vice Leader of the Ultrasound Imaging Team. Since October 2014, he has also been a junior member of the French Institut Universitaire de France. His research focuses on image and signal processing applied to medical ultrasound imaging. He is particularly interested in image formation techniques and motion estimation.

Mr. Liebgott has been an Associate Member of the IEEE Bio Imaging and Signal Processing (BISP) Technical Committee, and a member of the IEEE International Ultrasonics Symposium Technical Program Committee since 2014. He has been an Associate Editor of the IEEE TRANSACTIONS ON ULTRASONICS, FERROELECTRICS, AND FREQUENCY CONTROL since 2015.